Experimental constraints on melting temperatures in the MgO-SiO_2 system at lower mantle pressures

Marzena A. Baron[a,b*], Oliver T. Lord[b], Robert Myhill[b], Andrew R. Thomson[b,c], Weiwei Wang[b,c], Reidar G. Trønnes[a,d], Michael J. Walter[b]

a – Centre for Earth Evolution and Dynamics (CEED), University of Oslo, P.O. Box 1028 Blindern, Oslo, N-0315, Norway.

b – School of Earth Sciences, University of Bristol, Wills Memorial Building, Queens's Road, Bristol, BS8 1RJ, UK.

c – Department of Earth Sciences, University College London, Gower Street, London, WC1E 6BT, UK.

d – Natural History Museum, University of Oslo, P.O. Box 1172 Blindern, Oslo, N-0318, Norway.

Keywords: lower mantle; eutectic melting; diamond anvil cell; Early Earth Evolution; basalt; peridotite.

* Corresponding author:
Marzena Anna Baron - Tel: +47 22 85 62 54
E-mail address: m.a.baron@geo.uio.no / marzena.a.baron@gmail.com

Abstract

Eutectic melting curves in the system MgO-SiO_2 have been experimentally determined at lower mantle pressures using laser-heated diamond anvil cell (LH-DAC) techniques. We investigated eutectic melting of bridgmanite plus periclase in the MgO-$MgSiO_3$ binary, and melting of bridgmanite plus stishovite in the $MgSiO_3$-SiO_2 binary, as analogues for natural peridotite and basalt, respectively. The melting curve of model basalt occurs at lower temperatures, has a shallower dT/dP slope and slightly less curvature than the model peridotitic melting curve. Overall, melting temperatures detected in this study are in good agreement with previous experiments and *ab initio* simulations at ~25 GPa (Liebske and Frost, 2012; de Koker et al., 2013). However, at higher pressures the measured eutectic melting curves are systematically lower in temperature than curves extrapolated on the basis of thermodynamic modelling of low-pressure experimental data, and those calculated from atomistic simulations. We find that our data are inconsistent with previously computed melting temperatures and melt thermodynamic properties of the SiO_2 endmember, and indicate a maximum in short-range ordering in MgO-SiO_2 melts close to Mg_2SiO_4 composition. The curvature of the model peridotite eutectic relative to an $MgSiO_3$ melt adiabat indicates that crystallization in a global magma ocean would begin at ~100 GPa rather than at the bottom of the mantle, allowing for an early basal melt layer. The model peridotite melting curve lies ~500 K above the mantle geotherm at the core-mantle boundary, indicating that it will not be molten unless the addition of other components reduces the solidus sufficiently. The model basalt melting curve intersects the geotherm at the base of the mantle, and partial melting of subducted oceanic crust is expected.

1. Introduction

Seismic velocity and density profiles of Earth's lower mantle as depicted in 1-D radially averaged models (Dziewonski and Anderson, 1981) are generally consistent with a peridotitic bulk composition. However, the exact proportions of the primary mineral phases, bridgmanite, ferropericlase, Ca-perovskite and possibly stishovite, are not yet uniquely constrained, and it is not known if the upper and lower mantle are compositionally similar, or if the lower mantle composition has a higher Si/Mg ratio due to a more chondritic primitive composition (e.g. Murakami et al., 2012) or through accumulation of mafic material via subduction. Seismology also reveals the presence of both small (e.g. Helffrich, 2006) and large-scale velocity anomalies (e.g. Garnero and McNamara, 2008) in the lower mantle. Large-scale features include two antipodal large low shear wave velocity provinces (LLSVP), as well as the more localized ultra-low velocity zones (ULVZ; Garnero and McNamara, 2008, Lay et al., 2008) just above the core-mantle boundary (CMB). Depending on their origin and mineralogical constitution, these structures may exert a strong control on the distribution and magnitude of heat flow at the CMB and, therefore, on the convective dynamics and evolution of the Earth (e.g. Nakagawa and Tackley, 2008; Torsvik et al., 2016).

One possible explanation for large-scale features in the deep lower mantle is mineralogical layering inherited from solidification of a deep global magma ocean during the earliest part of the Hadean Eon. Although geochemical arguments strongly preclude large-scale fractionation, segregation of bridgmanite-rich domains constituting up to ~15% of the lower mantle remain plausible (e.g. Walter et al., 2004; Liebske et al., 2005). Another possible mechanism is the continued accretion of subducted oceanic crust at the base of the mantle, and the potential for melting of that material at the CMB (e.g. McNamara and Zhong, 2005). Testing these possibilities requires a detailed knowledge of the melting behaviour of mantle materials at the extreme conditions of the lower mantle.

Recent experiments on natural peridotitic and basaltic compositions (Fiquet et al., 2010; Andrault et al., 2011; Nomura et al., 2014; Andrault et al., 2014; Pradhan et al., 2015) yield a range of solidus and liquidus temperatures at lower mantle pressures, and it is difficult to discriminate between the effects of bulk composition, the presence or absence of volatiles in starting materials, and the different melting criteria and detection techniques used to establish the melting curves. In this study, we focus on eutectic melting in the system MgO-SiO_2 in order to eliminate the complexity inherent in natural multi-component systems. The MgO-SiO_2 system describes ~95% of the mineralogy of peridotite and ~70% of basalt at lower mantle conditions. Importantly, because melting is eutectic, compositions can be chosen that produce large amounts of melt at an invariant melting temperature, facilitating greatly our ability to detect melting in experiments at extreme pressures and temperatures.

1.1 Previous Work in the System MgO-SiO_2 at Lower Mantle Pressures

Eutectic melting in the MgO-$MgSiO_3$ binary has been studied experimentally using the multi-anvil apparatus up to pressures of 26 GPa (Gasparik, 1990; Presnall et al., 1997; Liebske and Frost, 2012). There is good agreement between these studies that the bridgmanite + periclase = melt eutectic is located at ~2775 K at 25 GPa, and that the eutectic liquid becomes progressively enriched in MgO with increasing pressure. Liebske and Frost (2012) presented a thermodynamic model for eutectic melting in this system, and based on extrapolation predicted that the eutectic liquid composition becomes richer in MgO up to about 80 GPa (from ~57 mol% at 24 GPa to ~60 mol% at 80 GPa), at which point it maintains a nearly constant Mg/Si ratio that is close to model bulk silicate earth (BSE). Atomistic simulations in the MgO-SiO_2 system by de Koker et al. (2013) show a similar increase in MgO content from 58 to 60 mol% for the bridgmanite + periclase eutectic liquid throughout the lower mantle pressure range (25 – 135 GPa). These authors also simulated melting in the $MgSiO_3$-SiO_2 binary, and found a

reduction in the MgO content of the bridgmanite + stishovite eutectic liquid from 37 to 33 mol% over the same pressure range; the silica phase is either stishovite or modified stishovite in the $CaCl_2$ crystal structure (referred to as stishovite from here onwards).

No previous experimental studies have investigated eutectic melting in the MgO-SiO_2 system throughout the lower mantle pressure range. The melting curves of the unary compounds MgO, $MgSiO_3$ and SiO_2 have been investigated in the laser-heated diamond anvil cell (LH-DAC) at pressures between ~30 and 60 GPa (e.g. Shen and Lazor, 1995), and results from these studies are in broad agreement with corresponding melting curves calculated from atomistic simulations (Stixrude and Karki, 2005; de Koker and Stixrude, 2009; de Koker et al., 2013). The experimentally derived melting curve of bridgmanite (Zerr and Boehler, 1993 and Shen and Lazor, 1995), however, maintains a considerably higher dT/dP slope and less curvature than the computationally derived curve (de Koker and Stixrude, 2009 and Di Paola and Brodholt, 2016) through the 24-60 GPa pressure range.

In this study we performed double-sided laser-heated diamond-anvil cell experiments to constrain eutectic melting temperatures in the MgO-SiO_2 binary system up to 110 GPa. The two eutectics in the MgO-SiO_2 system are considered model analogues for the melting of the natural lower mantle candidate lithologies, peridotite and basalt, respectively.

2. Experimental and Analytical Methods

2.1 Starting Compositions

The compositions of the starting materials used in this study are listed in **Table 1**. In selecting starting compositions we aimed to be close to the eutectic melt composition in both the MgO-$MgSiO_3$ and $MgSiO_3$-SiO_2 binary systems, as predicted in the studies of Liebske and Frost (2012) and de Koker et al (2013). In the MgO-$MgSiO_3$

system we chose a composition with 58 mol% MgO, whereas in the $MgSiO_3$-SiO_2 system we chose two mixes, one with 40 mol% MgO and the other with 35 mol% MgO.

Table 1. Experimental starting compositions (in mol%)

Starting mixtures	SiO_2	MgO	Components*
$M_{58}S_{42}$	42	58	En + Fo
$M_{40}S_{60}$	60	40	En + SiO_2
$M_{35}S_{65}$	65	35	En + SiO_2

*En: enstatite glass ($MgSiO_3$), Fo: crystalline forsterite (Mg_2SiO_4), SiO_2: silica glass

Fig. 1 shows our starting compositions relative to the predicted eutectic compositions derived from the atomistic computations of de Koker et al. (2013), and by applying the lever rule we calculate that our near-eutectic starting materials should yield from ~50% to 95% melt at lower mantle pressures. Producing such a large liquid fraction upon melting aids considerably in melt detection during laser heating and therefore enables higher precision on eutectic temperature assessment.

The MgO-$MgSiO_3$ binary composition was made by mixing enstatite glass with crystalline forsterite in the desired proportions, followed by grinding in an agate mortar under ethanol to a powder with a grain size of ~1 μm. Enstatite glass was made from a 1:1 molar mix of pure MgO and SiO_2 oxides, which were fused three times at 1 atm and ~1700 °C for 30 minutes. The pure, crystal free glass product was ground after each fusion to a very fine powder. Crystalline forsterite was synthesized from a 2:1 molar mix of pure MgO and SiO_2 oxides, which were sintered three times at 1 atm and 1500 °C for one hour and was verified as a pure phase by X-ray diffraction. The $MgSiO_3$-SiO_2 binary compositions were made by mixing enstatite glass (prepared as above) and high purity optical-grade silica glass (99.997%) in the desired proportions followed by grinding in an agate mortar under ethanol to a powder with a grain size of ~1 μm. Before weighing, all powdered components were dried at 120 °C and stored in a desiccator to prevent adsorption of water. To provide an absorber for the IR laser radiation, ~10 wt% of sub-micron tungsten powder was added to each starting composition. These mixtures were

then further ground in an agate mortar under ethanol to ensure that the W absorber was homogeneously distributed throughout the sample on the micron scale to provide as uniform heating as possible. All mixtures were stored at 120 °C under vacuum before use.

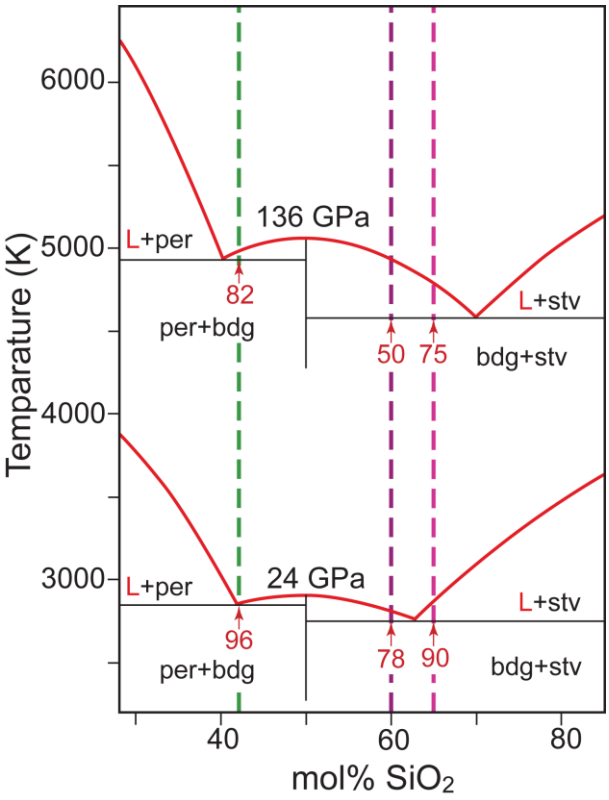

Fig. 1. Liquidus phase relations in the MgO-SiO_2 system at 24 and 136 GPa, adopted from de Koker et al. (2013). The initial fractions of eutectic melt (in percent) for the bulk starting compositions at 42, 60 and 65 mol% silica are calculated by the lever rule and shown beneath the red arrows representing the three starting compositions. Bdg = bridgmanite, per = periclase, stv = stishovite and L = liquid.

2.2 LH-DAC Experiments

2.2.1 High Pressure generation

High-pressure experiments were performed in 'Princeton-type' symmetric DACs, using Type Ia diamond anvils with culet diameters of 120, 150, 200 or 250 μm. Re gaskets were pre-indented to ~30 GPa and sample chambers were drilled by UV laser ablation in each indentation. We drilled multiple sample chambers in a single Re-gasket where space allowed; 3 holes when using 200 μm diameter culets for pressures of 60-90 GPa, and 4 holes when using 250 μm diameter culets for pressures of 24-60 GPa (Walter et al., 2015; Thomson et al., 2014). The initial sample chamber diameters were 25-30 μm, and all sample chambers drilled in one gasket were filled with the same starting material. Before sealing and pressurising, the loaded DAC was heated at 125 °C under Ar gas flow for at least one hour to remove adsorbed water and then closed at the same high temperature conditions.

We opted not to use an additional thermally insulating material between the sample and the diamond anvils in order to avoid chemical reactions and mechanical effects at high pressures (e.g. sample tearing and separation) that might affect the observed melting temperatures. This is especially important as we have designed the bulk compositions to produce high melt fractions at the invariant temperature to aid in melt detection.

2.2.2 Pressure Measurement

Pressure was determined on the basis of the Raman shift of the singlet peak related to stress in the (001) direction at the diamond culet surface (Hanfland et al., 1986), and is calibrated relative to the ruby fluorescence scale of Mao et al (1986) (see Walter et al., 2015). Confocal Raman measurements were made using a Jobin-Yvon T64000 Raman microscope at a spectral resolution of ~0.4 cm^{-1} within a diffraction limited focal volume. The calibrations based on diamond peak-shift are shown in **Figure S1** in the supplementary information. In each experiment, pressure was directly measured on each sample chamber before and after laser-heating. All reported

pressures in this study are post-heating measurements. No correction has been made for thermal pressure during heating due to lack of *in situ* EoS data. The thermal effect on pressure is not expected to be more than ~10% of the initial pressure measured at room temperature (Fiquet et al., 2010 and Andrault et al., 2011). None of the results reported here came from heating of the sample chambers that contained ruby as it was added only for the purpose of pressure calibration.

2.2.3 Laser Heating

Double-sided laser heating was performed at the University of Bristol using two 100 W Yb-doped fiber lasers (λ=1070 nm) combined with beam-shaping and beam-expanding optics to minimise radial temperature gradients. Beams were shaped to an approximately 'flat-top' energy distribution, with the spot size matched as closely as possible to the diameter of the sample chamber. The melting experiments were heated using an automated 'ramp mode', in which the laser power is continually and automatically increased by ~0.2 watts on each side every 4-6 seconds until quenching, resulting in a heating rate of 500-1500 K/min. We also performed a series of subsolidus experiments, where samples were heated to target temperatures below our melting curve and maintained at that temperature for ~30 minutes before quenching.

2.2.4 Temperature Measurement

At each step, temperatures were measured using standard spectroradiometric techniques (e.g. Walter and Koga, 2004). The thermal emission spectra were measured on both sides of the sample simultaneously over a wavelength range of 570 - 830 nm along an approximately 2 μm wide strip across the sample. Spectral intensity profiles were converted to temperatures by normalising to a NIST calibrated W-lamp of spectral radiance, with spectra fitted to the idealised grey-body Wien function. Maximum

temperature precision is achieved by selecting the best-fit 200 nm bandpass within the 570 - 830 nm window that minimizes the average analytical error on the fits; temperature precision is typically better than 10 K at 3000 K. Uncertainty in temperature accuracy related to possible wavelength dependent sample emissivity (e.g. non-grey body behaviour) is unknown. A boxcar smoothing procedure was performed on all temperature profiles to eliminate artefacts that arise because the spatial resolution of the CCD at the object plane (~1 μm) is smaller than the actual system optical resolution of ~3 μm. For more details on the laser heating and temperature measurement system employed here, including calibration, benchmarking and uncertainties, see Lord et al. (2014a).

In several experiments we also obtained 2D temperature maps using four-color imaging radiometry similar to that described in Campbell (2008). In brief, a 50x image of the sample is focussed onto a large format, high resolution CCD (SBIG Model ST-402ME) at four different wavelengths (550, 650, 750 and 850 nm). The images are superimposed in software to a precision of ± 1 pixel. Temperature is calculated from a four-color Wien fit at each pixel, with spectral intensity calibrated as described above for the 1D spectroradiometry system.

2.3 Analytical Methods

After decompression, the culet region of the gaskets were cut out by UV laser ablation, transferred to a 1-inch epoxy mould and embedded in standard epoxy. The cured epoxy discs were polished axially to expose the approximate centre of the sample chambers, first manually using water based 9 μm diamond suspension on a polishing cloth, and later using a Buehler EcoMet® grinder-polisher with 3 μm and 1 μm diamond suspension. Because the samples were very thin (~10 – 25 μm) and usually not completely flat after decompression, approximately 50% of all the sample chambers were lost during this process. Successfully polished samples were coated with a thin

layer of carbon or gold and analysed using a JEOL JXA8530F Field Emission Gun Electron Microprobe at the University of Bristol. Textural and chemical analyses were carried out with beam conditions of 5 keV and 20 nA. Wave-length dispersive elemental calibration was performed with the following standards: Si - synthetic SiO_2 crystal, Mg – synthetic MgO crystal, Al - Amelia albite and W - tungsten metal.

3. Results

3.1 Melt Detection: Thermal Signal Processing

Perturbations in the temperature-power relation as laser power increases have been shown to be an extremely robust indicator of melting. These perturbations commonly manifest as a distinct plateau in temperature as laser power increases; temperature plateaus are especially well defined during invariant melting of metals, but have also been used to effectively detect melting in low-variance silicate, silicate-carbonate, and silicate-water systems (e.g. Shen and Lazor, 1995; Anzellini et al., 2013; Lord et al., 2014a; Thomson et al., 2014; Walter et al., 2015). A comprehensive understanding of the factors resulting in thermal signal perturbations related to phase changes is elusive due to the diabatic nature of the sample environment and a lack of knowledge of material specific factors including changes in optical, thermal and mechanical properties upon crystallisation and/or melting (see for example: Geballe and Jeanloz, 2012; Lord et al., 2014a,b). Critically, this method has been corroborated using independent techniques, including direct observation of melt by *in situ* X-ray diffraction, often simultaneously (e.g. Anzellini et al. 2013; Lord et al. 2014a,b).

In all automatically ramped experiments, temperature was measured continuously at ~5s intervals during the heating ramp. We observe in some cases the appearance of a well-defined plateau in temperature as power continues to increase (**Fig. 2a**-**c**), but also commonly observe a rapid rise in temperature to a distinct temperature maximum that occurs after a gradual rise in temperature (**Fig. 2d**-**f**). These

perturbations are likely a consequence of the indirect heating of the silicate due to laser absorption by the dispersed W particles and mechanical segregation of a high-degree melt and W particles. We observe the temperature maxima at these perturbations to be pressure dependent, and we correlate these with eutectic melting of the sample. Textural observations support this interpretation.

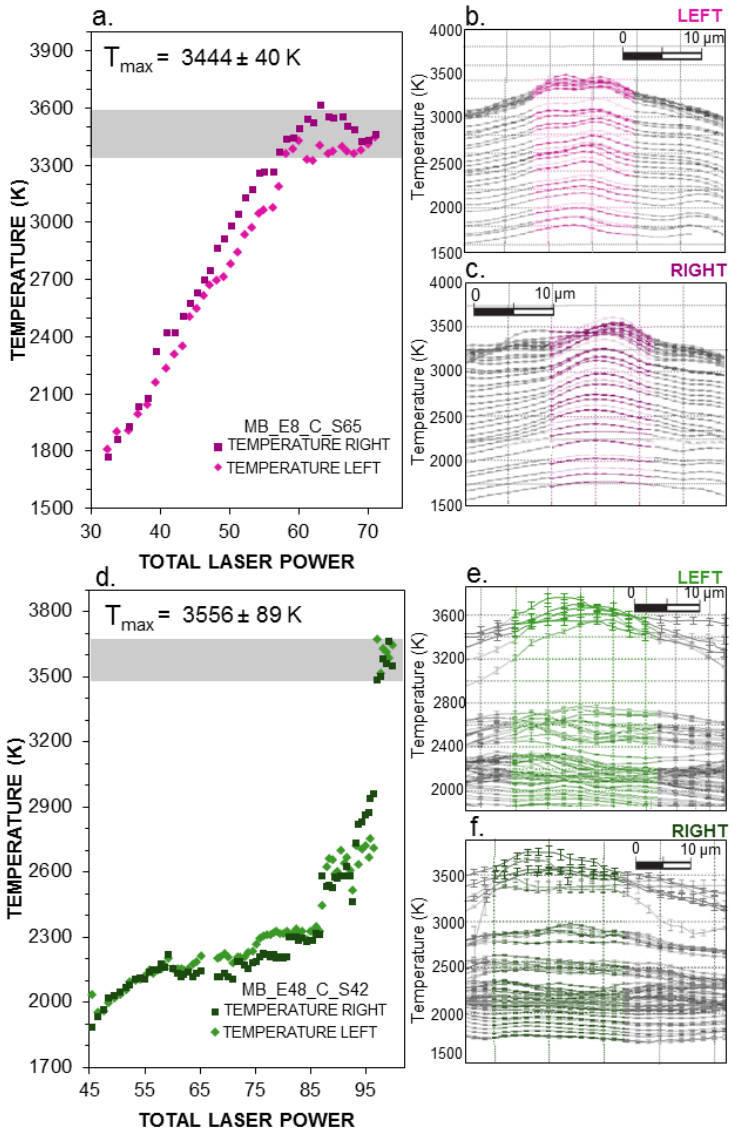

Fig. 2. Example of automatically ramped melting experiments showing: **(a)** Peak temperatures measured on the right (purple squares) and left (pink diamonds) sides of the DAC vs. total laser power in experiment MB_E8_C, and showing a well-developed temperature plateau. The pale grey band represents a 1 σ uncertainty in the mean of the points within the plateau (defined by the grey band); **(b, c)** temperature profiles across the heated spot recorded on both sides of the DAC for experiment MB_E8_C. The ranges

highlighted in colour reflect the selected windows used to define peak temperature. The sample chamber size is approximately 30 μm and the selected window is about 15 μm. Error bars reflect the precision of the Wien fits and are ±1σ; **(d)** Peak temperatures vs. laser power for experiment MB_E48_C showing a rapid increase in temperature before reaching a maximum temperature plateau; **(e, f)** temperature profiles across the heated spot for MB_E48_C.

3.2 Melting Detection: Textural Analysis

Textural and compositional analysis of recovered samples using backscattered electron imaging (BSE) and elemental mapping provide additional evidence for melting. To establish the baseline subsolidus texture, experiments were made well below the expected melting temperatures and at conditions approaching the solidus (**Tables S1** and **S2** in supplementary materials). All subsolidus samples we inspected using BSE imaging showed a relatively uniform distribution of W particles embedded in the silicate matrix, with no obvious indication of melting in the heated area (**Fig. 3a,b**). However, we do observe a distinct coarsening of the W grains at higher temperatures approaching the solidus (**Fig. 3b)**. In sharp contrast, samples where melting was detected by thermal signal processing show a range of textures consistent with melting, typical examples of which are shown in **Fig 3c**. The samples show segregation of W grains into a ring, or in a radial geometry about a central region that is relatively W-free. We also commonly observed a more centrally located large W aggregate (**Fig. 3c)**. We suggest that once a large melt fraction forms at the eutectic temperature, W grains are mechanically displaced by the melt, resulting in the observed segregation of silicate melt pool and W aggregates. Melt-W segregation may also provide at least a partial explanation for the increased power needed to maintain constant temperature at the eutectic.

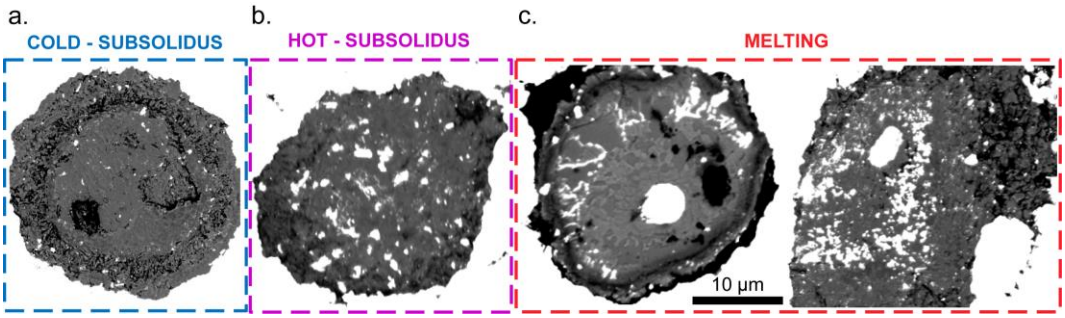

Fig. 3. BSE images of recovered DAC samples from: **(a)** cold-subsolidus (MB_E44_B P = 53.3 GPa and $T_{max,s}$ = 2350 K), **(b)** hot-subsolidus (MB_E36_C P = 36.7 GPa and $T_{max,s}$ = 2500 K), and **(c)** melted experiments (left: MB_E11_B P = 43.7 GPa and T_m = 2930±124 K, right: MB_E3_C P = 28.6 GPa and T_m = 2753±35 K).

The formation of a central aggregate and radially distributed W could indicate melting of the W absorber. However, we are confident that our melting curves represent the melting of the silicate rather than the W absorber because the 1 atm melting point of W (3687 K; Handbook of Physics and Chemistry) is considerably higher than most of our melting data. Another possibility is melting of the absorber as a consequence of carbide formation by reaction with the diamond. This is also an unlikely explanation as we observe no carbide formation in our electron probe analyses (W grains and/or aggregates are made of pure W), and the diamond anvil culet surfaces show no indications of reaction with the sample. Moreover, the melting point of tungsten carbide at 1 atm (3003–3103 K, Sittig's Handbook of Toxic and Hazardous Chemicals and Carcinogens) is higher than most of our data points below 40 GPa for the MgO-rich eutectic and 60 GPa for the SiO_2-rich eutectic, and as we will show below, our melting data at the lowest pressures investigated are consistent with results from multi-anvil apparatus experiments and *ab initio* simulations.

3.3 Melt Detection: Chemical Analysis

Polished samples were analysed with the electron probe to generate high-resolution X-ray elemental maps for Si, Mg and W, as well as spot chemical analyses. **Fig. 4** shows an example using the $M_{35}S_{65}$ starting material, where samples were pressurized

to almost identical pressure (~50 GPa) but heated to different temperatures. **Fig. 4a** shows a sample heated to 2000 K for 35 minutes, and **Fig. 4b** represents a sample heated to 2300 K for several minutes. Both samples show a relatively uniform distribution of W, indicating the samples remained subsolidus.

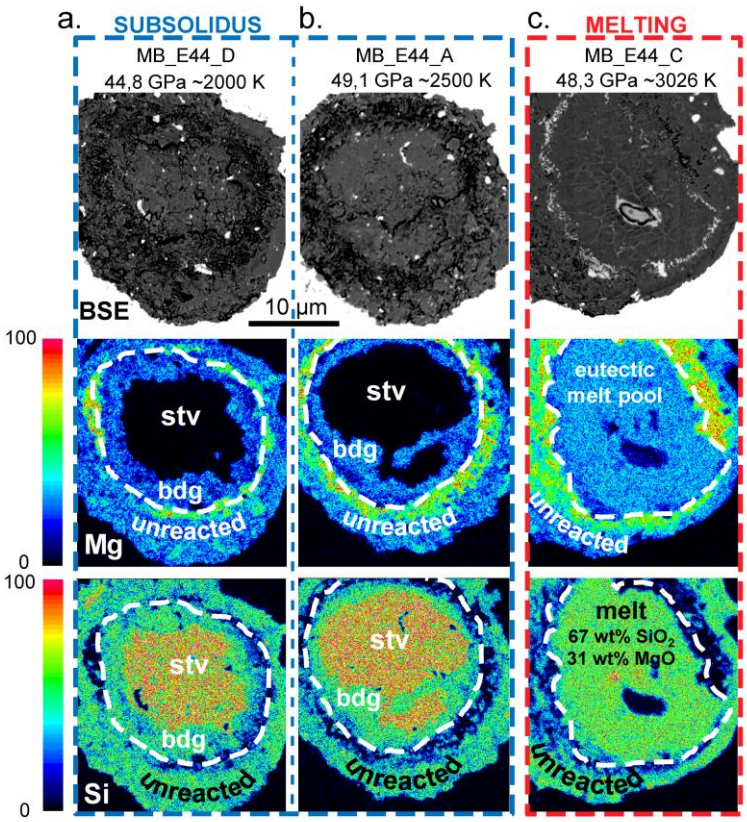

Fig. 4. Backscattered electron images (BSE) and wavelength dispersive elemental maps for Mg and Si of run products in the $MgSiO_3$-SiO_2 sub-system. **(a,b)** Two subsolidus samples (MB_E44_D and A) showing a homogeneous distribution of W grains in the BSE images, and phase segregation between bridgmanite (bdg) and stishovite (stv) in the heated region. **(c)** The melted sample (MB_E44_C) shows the typical annulus of W grains and a central aggregate in BSE, whereas the heated region shows a single homogeneous silicate with a composition close to that of the starting eutectic composition (67 wt% SiO_2 and 31 wt% of MgO), which we interpret as quenched melt

The Si- and Mg-chemical maps and spot analyses indicate the presence of two phases in the heated region, one of pure SiO_2, which we interpret as stishovite, and one with an intermediate Mg/Si ratio consistent with bridgmanite (the grains were too small

<500 nm for individual mineral analyses). The sample shown in **Fig. 4c** (MB_E44_C) was heated in ramp mode with melting detected by thermal signal processing at 3026 ±178 K at 48,3 GPa. Here again, we observe the typical W-ring around the quenched melt pool and also a W-aggregate in the middle. The Si- and Mg-elemental maps show a large, chemically homogeneous central area with an Mg/Si ratio intermediate between bridgmanite and stishovite, indicative of a quenched eutectic melt. We performed chemical mapping like that shown in **Fig. 4** on a number of samples in both the MgO-$MgSiO_3$ and $MgSiO_3$-SiO_2 systems, with similar and consistent results. The textural and chemical analyses fully support the interpretation from thermal signal processing of sample melting.

The subsolidus chemical maps (**Fig. 4a,b**) show phase separation between bridgmanite and stishovite , which is likely due to Soret or saturation gradient diffusion in response to the temperature gradient through the sample (e.g. Sinmyo and Hirose, 2010). We observe SiO_2 crystallizing within the hottest region, with bridgmanite intergrown or forming an annulus around stishovite, consistent with SiO_2 diffusing to the hot region. Temperature gradient induced phase segregation is also common in multi-anvil experiments where the temperature gradients are much less extreme (e.g. 100 C/mm), and have been reported previously to occur in the MgO-SiO_2 system (Presnall and Walter, 1993).

3.4 2D - Sample Temperature Distribution

The radial temperature distribution, as measured by 2-D imaging radiometry, varies in detail from sample to sample but has common features. **Fig. 6** shows two examples, one showing a subsolidus temperature distribution (**Fig. 5a**), and another showing the temperature distribution after a temperature-power perturbation interpreted as melting (**Fig. 5b**). In the subsolidus we commonly observe a ~15 μm diameter region with roughly constant temperature (~±50 K), surrounded by a region

where temperature decreases with increasing distance from the centre at ~20-30 K/μm, mimicking the energy distribution of the incident laser radiation. This gradient continues up to the radius at which the intensity of the incandescent light drops to ~10% of the maximum and an accurate temperature fitting becomes impossible (the dark blue region in **Fig. 5**). This masks the steep gradient of ~10^3 K/μm that defines the edge of the laser heated region. Such a temperature distribution is stable for extended duration (e.g. tens of minutes). However, with continuous increase in laser power and temperature, we observe a drastic, time-dependent change in temperature distribution (e.g. **Fig. 5b**) that correlates with the melting perturbation (plateau). **Fig. 5b** shows a central temperature peak and an annulus of high temperatures separated by a slightly cooler zone that mimics closely the distribution of W typically observed upon melting of the sample (**Fig. 3 and 4**).

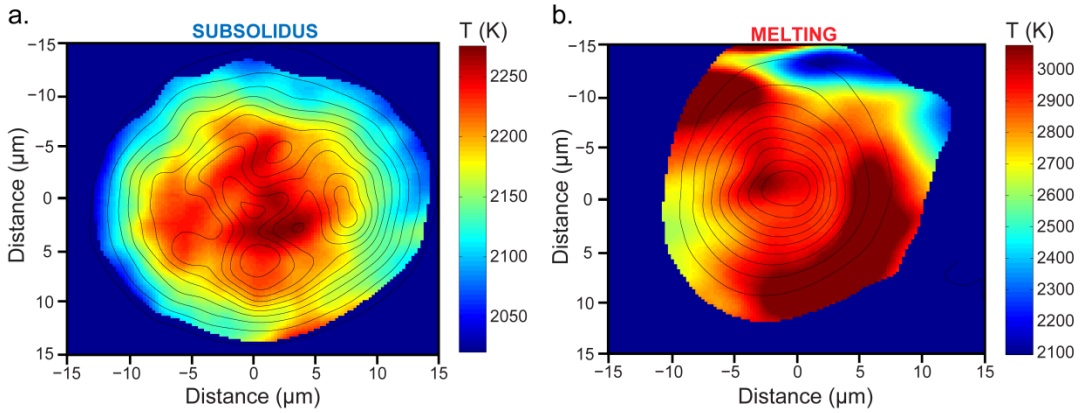

Fig. 5. 2-D temperature maps over the laser-heated region in LH-DAC experiment MB_48_C at 48.3 GPa as determined using 4-color imaging radiometry. **(a)** Subsolidus temperature map collected at the beginning of laser-heating at ~2300 K. **(b)** Super-solidus temperature map collected just before quenching at ~3000 K. Contour lines represents light intensity relative to the maximum at intervals of 10%. The dark blue regions are not fitted because of insufficient light intensity that coincides with the very steep temperature gradient (~10^3 K/μm) separating the laser heated region from its unheated surrounding. See text for more details.

An axial temperature gradient must also be present between the diamond anvils over a thickness of ~10–25 μm (depending on pressure), but is not well defined because we cannot measure it directly. We expect an ~5 – 10 μm region in the centre across which temperature decreases at the modest rate (~±50 K/μm), and a steep gradient over a few microns toward the highly thermally conductive diamond surfaces on each side.

3.5 Melting Curves

The melting temperatures reported in this study are calculated as the mean of the smoothed maximum temperatures ($T_{max,s}$ data in **Table S1** and **S2 in supplementary materials**) from both sides of the sample, from the start of the temperature plateau until quenching. The reported uncertainties include the analytical precision in the greybody spectral fitting and one standard deviation of the temperature variation within the melting plateau, which results in total uncertainties of ~50 – 300 K. We do not include an uncertainty related to non-greybody sample emissivity. Similarly, in subsolidus experiments we report temperatures calculated as the mean of the measured maximum temperatures on both sides of the sample, starting from the power at which the target temperature was reached until quenching. The run conditions of melting and subsolidus experiments are listed in **Tables S1** and **S2** in the supplementary materials and the results are plotted in **Fig. 6**.

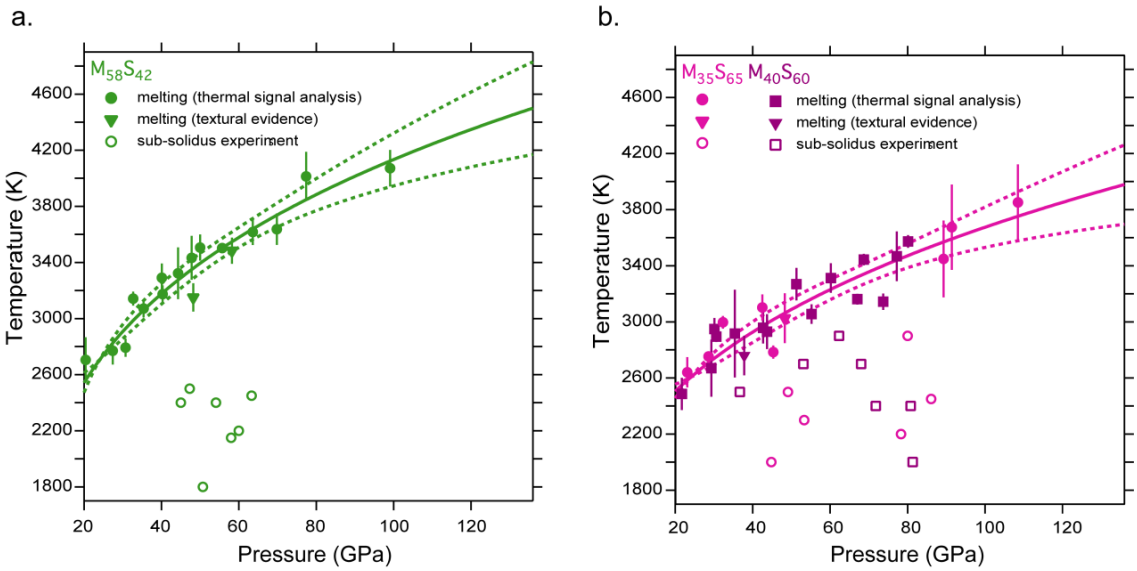

408

409 **Fig. 6.** Results of this study for **(a)** the MgO-$MgSiO_3$ eutectic ($M_{58}S_{42}$), and **(b)** the
410 $MgSiO_3$–SiO_2 eutectic ($M_{35}S_{65}$ and $M_{40}S_{60}$). The melting curves (solid lines) are fitted
411 using a modified Simon-Glatzel equation (Simon and Glatzel, 1929) with parameters
412 listed in **Table S3** and extrapolated to 136 GPa with associated 95% confidence
413 intervals (dashed lines).

414 All ramped experiments that resulted in detectable melting plateaus were used
415 to constrain the melting curves. We could not detect any statistical difference between
416 the melting data for the two Si-rich compositions we studied in the $MgSiO_3$-SiO_2 system,
417 as expected for a eutectic system. Therefore, we fitted all the data simultaneously to
418 produce a single eutectic melting curve. The P-T data are fitted using a modified Simon-
419 Glatzel equation:

$$T_m = T_{24}\left(1 + \frac{P_m}{A}\right)^{\frac{1}{C}} \quad (1)$$

420 where T_m is the melting temperature at pressure P_m, A and C are fitting parameters (see
421 **Table S3** in supplementary materials), and T_{24} is the melting temperature at 24 GPa
422 from this study, which is consistent with both Liebske and Frost (2012) and de Koker et
423 al. (2013). Because the lower mantle mineral assemblages differ from those at ambient
424 pressure conditions, we use T_{24} as the starting point for our fits rather than the
425 commonly used T_0 in the original Simon-Glatzel equation (Simon and Glatzel, 1929). The

reference melting temperature at 24 GPa (T_{24}) represents approximately the pressure at which bridgmanite becomes stable. The melting temperatures for the two eutectics can be fitted with curves with positive and decreasing dT/dP slopes through the lower mantle pressure range.

4. Discussion

4.1 Comparison with Previous Work in the MgO-SiO_2 System

In **Fig. 7** we compare our experimentally determined eutectic melting curves with previously published results from atomistic simulations (de Koker et al., 2013), previous experiments, thermodynamic modelling (Liebske and Frost, 2012), and endmember melting temperatures for $MgSiO_3$ (Stixrude et al. 2009), SiO_2 (Shen and Lazor, 1995) and MgO (Alfé, 2005). Our MgO-$MgSiO_3$ eutectic melting curve is in excellent agreement with the experimental data of Liebske and Frost (2012) in the lower pressure range (24 – 26 GPa). However, at higher pressures our melting curve is systematically lower than their extrapolated melting curve predicted on the basis of thermodynamic modelling. The predicted melting curve of Liebske and Frost (2012) is a maximum of ~350 K higher than our curve; at the pressure of the core-mantle boundary it lies within our uncertainty envelope. The bridgmanite + periclase eutectic as calculated by de Koker et al. (2013) is higher than our curve by about 100 K at 24 GPa, and about 450 K at 136 GPa.

The liquidus diagram for the $MgSiO_3$-SiO_2 system at lower mantle pressures has not been previously studied experimentally. The first principles calculations of de Koker et al. (2013) in this system predict eutectic melting temperatures of about 2740 K and 4580 K at 24 and 136 GPa, respectively, which are about 230 K and 600 K above our melting curve at these pressures.

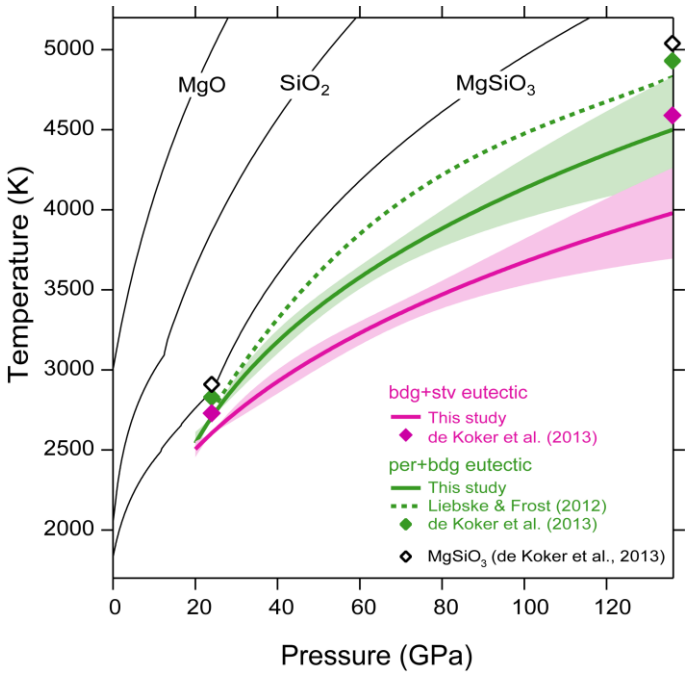

Fig. 7. Eutectic melting curves from this study (solid lines with shaded area) compared with results from atomistic calculations (solid diamonds - de Koker et al., 2013), thermodynamic modelling (dashed line - Liebske & Frost, 2012) and melting curves of endmembers $MgSiO_3$ (Stixrude et al. 2009), SiO_2 (Shen and Lazor, 1995) and MgO (Alfé, 2005). The green and pink melting curves represent the peridotitic ($M_{58}S_{42}$) and basaltic ($M_{35}S_{65}$ and $M_{30}S_{60}$) model eutectics, respectively. The model basalt melting curve has a lower dT/dP-slope and less curvature than the model peridotite melting curve throughout the lower mantle pressure range.

The systematically lower melting points in our work compared to the first principles calculations might be explained by the difficulty in obtaining accurate melting points (T_m) in polyatomic systems using *ab initio* molecular dynamics. Simulations of relatively small systems (66-78 atoms, de Koker et al., 2013) with periodic boundary conditions tend to overestimate T_m due to the lack of defects and surfaces on which melt can nucleate.

4.2 Comparison with Melting Curves of Natural Compositions

Fig. 8 compares our eutectic melting curves with experimentally determined solidi for natural basalts and peridotites. Eutectic melting curves in the MgO-SiO_2 binary

system should be higher than in systems that contain additional components. The multi-component peridotite solidi of Fiquet et al. (2010), Andrault et al. (2014) and Nomura et al. (2014) are shown in **Fig. 9a**. Fiquet et al. (2010) used a combination of X-ray scattering and textural evidence to detect melting in a model upper mantle composition (KLB-1), and found a solidus that is about 200 K lower than the bridgmanite + periclase eutectic determined here, but with an almost identical curvature. Andrault et al. (2011), also relying on X-ray diffraction and textural evidence for melt detection, found a solidus for model chondritic peridotite that has little or no curvature and which is located below the bridgmanite + periclase eutectic by a maximum of ~600 K at 80 GPa, but is within 300 K at the lower and higher pressure extremes. The pyrolitic peridotite solidus determined by Nomura et al. (2014) also has small curvature, but is about 1000 K below the bridgmanite + periclase eutectic at 80 GPa, and well below the other natural peridotite melting curves. Our peridotite melting curve is higher than those of natural compositions due to the reduction in temperature caused by the solution of additional components into the melt, with iron likely to have the most significant effect. For example, de Koker et al. (2013) suggest adding around 10 mol% Fe to the MS system would reduce the solidus by 250±50 K. Such a reduction would bring our melting curves into much closer agreement with those of Fiquet et al. (2010) and Andrault et al. (2011) in the peridotitic system, though the curvature would still more closely resemble the study of Fiquet.

The different melting temperatures observed among studies in multi-component systems must reflect compositional differences to some degree (e.g. Mg/Si ratio, H_2O content), but differences in melt detection criteria are also likely to be relevant. In natural systems melting occurs over a temperature interval, rather than at a eutectic temperature. The X-ray scattering techniques used in the studies of Fiquet et al. (2010) and Andrault et al (2011) (e.g. diffuse scattering; grain growth; phase disappearance) likely lead to overestimation of the solidus temperature because a substantial melt

fraction may need to be present before melt can be detected. Nomura et al. (2014) attribute their lower temperature solidus to a combination of more sensitive melt detection technique based on X-ray tomographic imaging, and to the presence of ~400 ppm H_2O in their starting composition.

The multi-component basalt solidi of Hirose et al. (1999), Andrault et al. (2014) and Pradhan et al (2015) are shown in **Fig. 8b**. Both Hirose et al. and Pradhan et al. use thermal signal processing as a primary melting criterion, their melting curves are nearly identical, and are supported at the low-pressure end by multi-anvil press (MAP) experiments. The melting curves from these studies have a nearly identical shape to the bridgmanite + stishovite eutectic curve found in our experiments, and lie close to our melting curve. This would suggest that addition of iron and other components has little effect on solidus temperature. However, in contrast, the basaltic solidus of Andrault et al. (2014), determined using X-ray diffraction and temperature plateaus as melting criteria, falls ~600 K below our bridgmanite + stishovite melting curve at 30 GPa, and ~300 K below at pressures greater than about 60 GPa. As with peridotite melting, melt detection in multi-component basaltic systems will depend on the melt fraction exceeding the detection limit. For example, in the study of Hirose et al., the basalt sample was 'sandwiched' between Re absorbers, and melting was detected by a rapid rise in temperature. It may be that melting occurs at a lower temperature, and the runaway heating occurs only after considerable melt is present such that the solidus temperature is overestimated.

We reiterate that the advantage of working in the MgO-SiO_2 system using near-eutectic starting compositions is that large amounts of melt are produced at a single eutectic temperature, allowing a more accurate determination of melting. In contrast, the melting curves produced in studies on natural compositions may represent the temperature at which the melt fraction exceeds the detection limit of the method used

for melt determination, whether it be thermal signal processing or *in situ* X-ray diffraction methods.

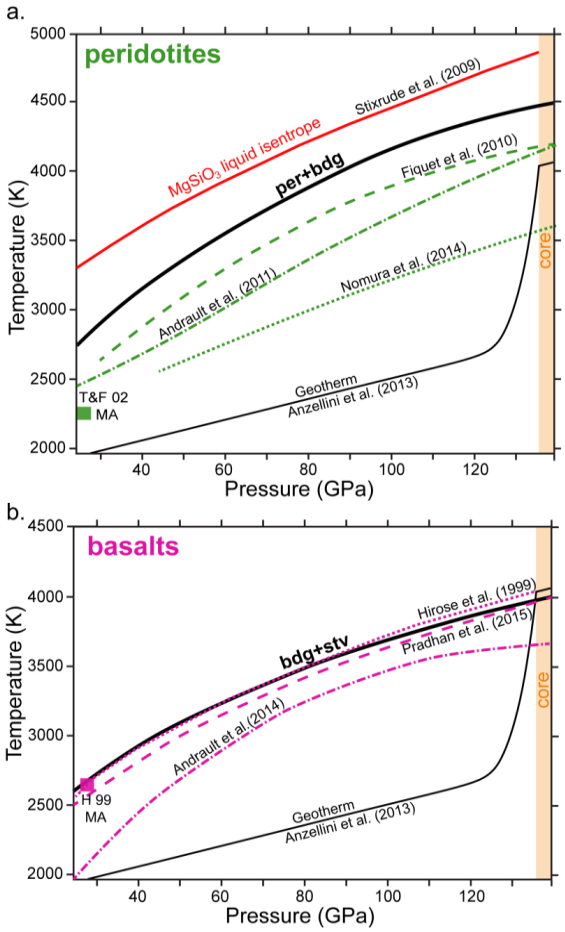

Fig. 8. A comparison of experimentally determined melting curves (thick black solid lines) in this study of: **(a)** the bridgmanite + periclaseeutectic compared with the peridotite solidi determined in LH-DAC experiments by Fiquet et al. (2010), Andrault et al. (2011), Nomura et al. (2014) and MAP experiments by: Trønnes and Frost (2002), together with the $MgSiO_3$ liquid isentrope from Stixrude et al. (2009); **(b)** the bridgmanite + stishovite eutectic compared with the basalt solidi determined in LH-DAC experiments by Hirose et al. (1999), Andrault et al. (2014) and Pradhan et al. (2015) together with a single MAP experiment from Hirose et al. (1999). The mantle adiabat of Anzellini et al. (2013, supplementary) is shown for comparison.

4.3 Implications for Thermodynamic Modelling of the MgO-SiO_2 System

The eutectic melting curves presented in this study provide constraints on the thermodynamic properties of the MgO-SiO_2 liquid solution. By employing *ab initio*

derived endmember models for the solids (periclase and stishovite) and liquids (MgO and SiO_2) from de Koker et al. (2013) and references therein, we calculated the activities (a_i) of MgO and SiO_2 in the two eutectic liquids using the equilibrium relation:

$$\mu_i = G_i^\circ + RT \ln a_i \quad (2)$$

where G_i° is the Gibbs free energy of component i (e.g. MgO or SiO_2) in the pure endmember melt and μ_i is the chemical potential of that component in the melt. At the bridgmanite + periclase eutectic, the chemical potential of MgO liquid is equal to the Gibbs free energy of periclase (assuming no SiO_2 is incorporated into periclase, Equation 2). The same is true of SiO_2 liquid and stishovite for the bridgmanite + stishovite eutectic (Equation 3). The thermodynamic relationships can be described as:

$$\mu_{MgO}^{liquid} = \mu_{MgO}^{solid} \quad (3)$$

$$\mu_{MgO}^{\circ,liquid} + RT \ln a_{MgO} = \mu_{MgO}^{\circ,solid} \quad (4)$$

and

$$\mu_{SiO_2}^{liquid} = \mu_{SiO_2}^{solid} \quad (5)$$

$$\mu_{SiO_2}^{\circ,liquid} + RT \ln a_{SiO_2} = \mu_{SiO_2}^{\circ,solid}. \quad (6)$$

As the resulting activities only rely on endmember properties, they can be used to assess the accuracy of MgO-SiO_2 solution models (**Fig. 9**). We demonstrate this by comparing our calculated activities with predictions from a Margules-like mixing model that reasonably reflects the *ab initio* results (de Koker et al., 2013) at lower mantle pressures (**Fig. 9**). Margules interaction parameters (W_i) in a asymmetric regular solution model describe and fit the excess Gibbs free energy of the binary liquid mixture (e.g. Thompson, 1967 and Haselton and Newton, 1980) as:

$$G_{mix} = G_{ideal} + W_A\, Y^2(1-Y) + W_B\, Y(1-Y)^2 \quad (7)$$

where $Y = \frac{X}{X+\lambda(1-X)}$ and $X = X(SiO_2)$ (molar fraction of SiO_2) so that $X = Y$ when $\lambda = 1$. However, de Koker et al. (2013) suggests using $\lambda = 1.43$, which allows for additional

555 asymmetry in G_{mix} and enables a match to their low pressure enthalpy of mixing data.
556 The resulting Margules parameters for the binary mixture are the following:

$$W_A = 80 \cdot 10^3 - 70T \quad (8)$$

$$W_B = -245 \cdot 10^3 - 25T \quad (9)$$

557 In **Fig. 9** we observe the pressure-driven increase in the activity of SiO_2 derived from the
558 de Koker et al. (2013) endmembers and bridgmanite + stishovite eutectic temperatures,
559 and at face value the indication is that bridgmanite + stishovite eutectic melts become
560 markedly more SiO_2-rich. Such a dramatic change in the bridgmanite + stishovite
561 eutectic composition would require a rapid change in melt solution properties at high
562 pressures, which seems unlikely, and so a different explanation is required. We note that
563 the calculated increase in silica activity is a direct consequence of the marked flattening
564 of the de Koker et al. (2013) SiO_2 melting curve at high pressures (based on first-
565 principles simulations by Karki et al., 2007; **Fig. S2a**), which is not mirrored in the
566 pressure dependence of bridgmanite + stishovite eutectic temperatures presented in
567 this study. Our results may thus indicate that the melting curve and properties of SiO_2
568 melt require reassessment. Especially as a number of ab initio studies note that
569 obtaining accurate thermodynamic properties of silica-rich solids and liquid remains
570 challenging due to a high degree of polarization and very slow diffusion of viscous liquid
571 silica (e.g. Tangney and Scandolo, 2002).

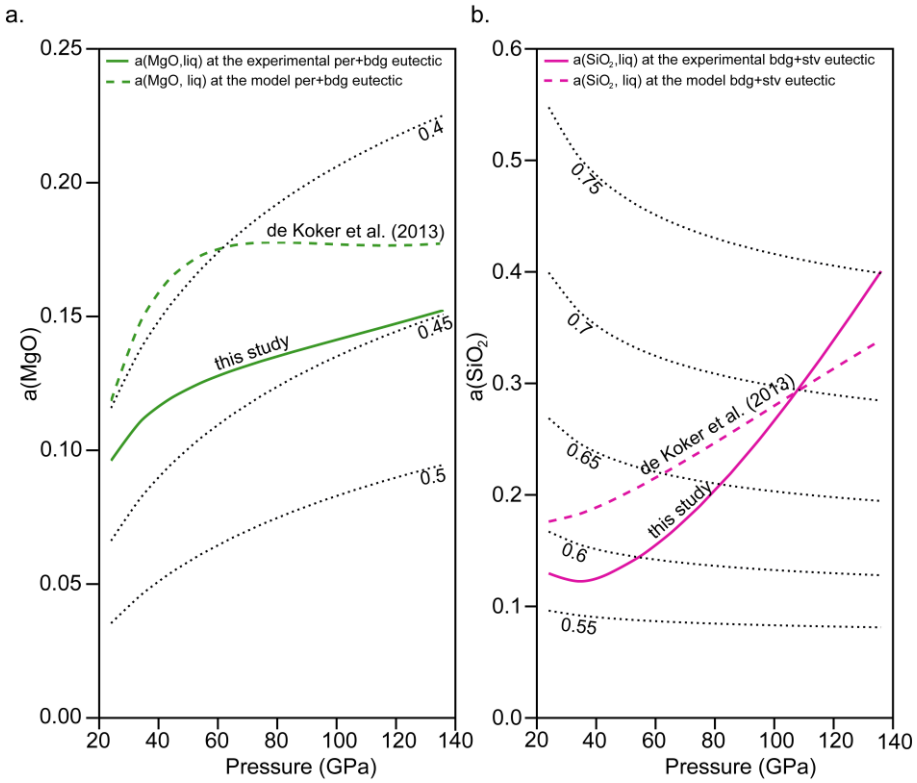

572

573 **Fig. 9.** A comparison between the activities of **(a)** MgO and **(b)** SiO_2 in eutectic liquids
574 calculated based on the thermodynamic model of de Koker et al. 2013 using
575 experimentally determined eutectic melting curves from this study (solid lines)
576 compared with previous estimates (dashed lines) which reflects the variation of
577 bridgmanite + periclase (green) and bridgmanite + stishovite (pink) eutectic
578 compositions with pressure. The dotted lines are calculated for different melt
579 compositions at the experimentally derived eutectic temperature, according to the
580 modified Margules mixing model described in the main text.

581 Our experimental results also provide considerable constraints on the mixing
582 properties of MgO-SiO_2 liquids. Specifically, the 100 – 500 K difference between the
583 bridgmanite + periclase and bridgmanite + stishovite eutectic temperatures is a
584 sensitive function of the shape of the free energy mixing curve. Although the results of
585 de Koker et al. (2013) produce similar temperature differences between the eutectics,
586 we note that this prediction is dependent on large entropies of mixing, coupled with a
587 model in which bridgmanite is about 40 kJ/mol more stable relative to periclase +
588 stishovite than in experimental datasets at 24 GPa (e.g. Stixrude and Lithgow-Bertelloni,
589 2011; Holland and Powell, 2011 **Fig. S2b**). If we assume instead that the experimentally

derived datasets provide accurate estimates of the free energy of the reaction bridgmanite = periclase + stishovite, then our eutectic melting curves tell two things about the mixing and endmember properties of the MgO-SiO_2 melt system. First, a low temperature bridgmanite + stishovite eutectic (relative to bridgmanite + periclase) indicates that SiO_2 melting temperatures are probably overestimated, at least at pressures corresponding to shallow parts of the lower mantle. Second, to ensure that melting of bridgmanite remains congruent despite a relatively low stability (relative to its constituent oxides), the minimum in the liquid Gibbs free energy of mixing must be quite angular and shifted to the MgO-rich side of bridgmanite. This angularity can be explained by a maximum in short range order around the Mg_2SiO_4 composition, which has been proposed on the basis of both theoretical considerations and low pressure experimental results (Wu et al., 1993; Harvey et al., 2015). This maximum implies that the activities of MgO and SiO_2 in ultramafic melts change quite abruptly as a function of silica content, which could strongly influence phase equilibria in a partially molten mantle.

4.4 Implications for Melting in the Deep Mantle

4.4.1 Crystallization of a Deep Magma Ocean

During the late stage accretion of Earth one or more giant impacts probably resulted in deep magma ocean(s) on a global scale (e.g. Benz and Cameron, 1990). Crystallization of a Hadean magma ocean would have set the initial state of the mantle, with crystal-melt fractionation potentially leading to large-scale early mantle heterogeneity. Near-equilibrium crystallisation of a magma ocean, as a result of efficient convective mixing of suspended crystals, would not be an effective fractionation mechanism (e.g. Solomotov and Stevenson, 1993). Fractional crystallization due to crystal settling or floating, or liquid segregation and trapping due to negative buoyancy could, however, lead to extensive primordial differentiation. The density contrast

between crystals and liquid is therefore a key parameter controlling magma ocean evolution. Another important factor is the depth at which the magma ocean begins to crystallize, which depends on the relationship between the magma ocean adiabatic temperature gradient and the slope of the peridotite liquidus.

First principles molecular dynamics simulations of melts in the $MgSiO_3$ system (Stixrude and Karki, 2005; Stixrude et al., 2009) show that the liquid adiabat, due to a continuous increase in the Gruneisan parameter of the liquid with pressure, is steeper than the melting curve, such that crystallization should begin in the middle of the lower mantle, rather than from the bottom up. On the basis of the shape of the bridgmanite + periclase eutectic curve found here, and assuming that the $MgSiO_3$ liquid adiabat is an adequate representation of the more MgO-rich eutectic liquid, the adiabat would intersect the melting curve at about 100 GPa (**Fig. 8a**). That is, our eutectic curve is consistent with crystallization beginning deep within a global magma ocean, but not at the bottom. However, the shape of the melting curve above 110 GPa is an extrapolation of the fit of the experimental data obtained at lower pressures.

A middle-outward style of crystallization creates the potential for residual melts to become trapped near the bottom of the lower mantle forming a 'basal magma ocean', the remnants of which may manifest themselves in the modern Earth as seismic low velocity structures (LLSVP, ULVZ) (e.g. Labrosse et al., 2007). The melt-solid density difference will determine the fate of the basal liquid. Petitgirard et al. (2015) measured the density of amorphous $MgSiO_3$ at high pressures, and predicted a very small density contrast between crystalline and molten bridgmanite. With the strong preference for iron to partition from ferropericlase and bridgmanite into melt relative to magnesium (e.g. Tateno et al., 2014; Pradhan et al., 2015; Boukaré et al., 2015) it is probable that a melt-solid density cross-over exists in the lower mantle, and that basal melt derived from mid-mantle magma ocean crystallisation would remain negatively buoyant.

4.4.2 Melting of Peridotite and Basalt at the CMB

The mantle adiabat by Anzellini et al. (2013) extended to an outermost core temperature of 4050 K, is shown in **Fig. 8**. The bridgmanite + periclaseeutectic melting curve (model peridotite) does not intersect the adiabat, so melting would not be predicted to occur at the base of the modern mantle based on the simplified system. The melting curves of Fiquet et al. (2010) and Andrault et al. (2011) also lie just above the adiabat at the CMB, although within uncertainty. Only the melting curve of Nomura et al. (2014) lies clearly below the adiabat such that melting at the base of the mantle is predicted to occur.

In contrast, our bridgmanite + stishovite melting curve (model basalt) intersects the mantle adiabat just above the core-mantle boundary, as do all melting curves for natural basalt. This region above the CMB is where localised but significant reductions in both P- and S- wave velocities are observed in seismic data (e.g. Williams and Garnero, 1996, Garnero and Helmberger, 1998). Thus, partially molten recycled basalt is considered a possible candidate material for the thin ultra-low velocity zones (ULVZs) located directly above the outer core surface (e.g. Andrault et al., 2014; Pradhan et al., 2015). Subducted oceanic crust is slightly denser than the ambient peridotite (e.g. Ballmer et al., 2015) and may partially segregate downwards in the low-viscosity D" zone during conductive heat transfer from the outer core and lateral flow towards the LLSVPs (Torsvik et al., 2016). Basaltic material near the bottom of the D" flow may interact and replenish the ULVZs, which are frequently confined to LLSVP-margins (e.g. Thorne and Garnero, 2004). Moreover, most deep plumes seem to be rooted near the edges of the LLSVPs and therefore may partially entrain basaltic material from the ULVZs (French and Romanowicz, 2015; Torsvik et al., 2016).

5. Conclusions

Eutectic phase relations in the system MgO-SiO_2 involving the assemblages bridgmanite + periclase + melt and bridgmanite + stishovite + melt provide analogues for melting of peridotite and basalt at lower mantle conditions, respectively. Our experimental melting curves from ~20-110 GPa provide constraints on the maximum melting temperatures in peridotitic and basaltic lithologies relevant to the Earth's mantle. The bridgmanite + periclase (peridotite) melting curve is ~100 K higher at the top of the mantle than the bridgmanite + stishovite (basalt) melting curve, but is ~500 K higher at the CMB. The bridgmanite + periclase eutectic curve has a shape indicating that a deep, peridotitic global magma ocean would begin crystallizing at ~100 GPa, favouring the possibility of residual, basal melt layer at the base of the mantle. Relative to estimates of the mantle geotherm, our data indicate that basalt will melt near the core-mantle boundary. The model peridotite eutectic is about 500 K higher than the mantle geotherm at the core-mantle boundary, but melting may occur due to the depression of the solidus caused by additional components (e.g. FeO, CaO, Al_2O_3, Na_2O).

Acknowledgements

This work was mainly supported by The Centre for Earth Evolution and Dynamics, founded by the Centre of Excellence grant (project number 223272) from the Research Council of Norway. MAB also thanks the Faculty of Mathematics and Natural Sciences, University of Oslo, for Kristine Bonnevie scholarship in 2014 and 2015. OTL would like to acknowledge support from NERC through a postdoctoral research fellowship (NE/J018945/1). MJW acknowledges support for this work from NERC grant (NE/I010947/1). Ben Buse and Stuart Kearns are thanked for assistance with FEG microprobe analyses. We also thank Julien Siebert and Daniel Frost for constructive reviews, and Frederic Moynier for the editorial handling of our manuscript.

References

Alfé D., 2005. Melting Curve of MgO from First-Principles Simulations. Phys. Rev. Lett. 94, 235701.

Anzellini, S., Dewaele, A., Mezouar, M., Loubeyre, P., Morard, G., 2013. Melting of iron at Earth's inner core boundary based on fast X-ray diffraction. Science 340 (6131), 464-466.

Andrault, D., Bolfan-Casanova, N., Nigro, G.L., Bouhif, M.A., Garbarino, G., Mezouar, M., 2011. Melting curve of the deep mantle applied to properties of early magma ocean and actual core-mantle boundary. Earth Planet. Sci. Lett. 304, 251-259.

Andrault, D., Pesce G., Bouhifd, M.A., Bolfan-Casanova, N., Hénot, J.-M., Mezouar, M., 2014. Melting of subducted basalt at the core-mantle boundary. Science 344 (6186), 892-895.

Ballmer, M.D., Schmerr, N.C., Nakagawa, T., Ritsema, J., 2015. Compositional mantle layering revealed by slab stagnation at ~1000-km depth. Sci. Adv. 1, 1-9.

Benz W., Cameron A., G., H., 1990. Terrestrial effects of the Giant Impact. In: Newsom HE & Jones JH (eds.), New York: Oxford University Press, Origin of the Earth, 61-67.

Boukaré, C.-E., Ricard, Y., Fiquet, G., 2015. Thermodynamics of the MgO-FeO-SiO2 system up to 140 GPa : application to the crystallization of Earth's magma ocean. J. Geophys. Res. Solid Earth 120, 6085-6101.

Campbell, A.J., 2008. Measurement of temperature distributions across laser heated samples by multispectral imaging radiometry. Rev. Sci. Instrum. 79, 015108.

de Koker, N., Strixrude, L., 2009. Self-consistent thermodynamic description of silicate liquids, with application to shock melting of MgO periclase and $MgSiO_3$ perovskite. Geophys. J. Int. 178, 162–179.

de Koker, N., Karki, B.B., Stixrude, L., 2013. Thermodynamics of the MgO–SiO_2 liquid system in Earth's lowermost mantle from first principles. Earth Planet. Sci. Lett. 361, 58-63.

Di Paola, C., Brodholt, J.P., 2016. Modeling the melting of multicomponent systems: the case of $MgSiO_3$ perovskite under lower mantle conditions. Sci. Rep. 6, 29830.

722 Dziewonski, A.M., Anderson, D.L., 1981. Preliminary reference Earth model. Phys. Earth
723 Planet. Inter. 25(4), 297-356.

724 Fiquet, G., Auzende, A.L., Siebert, J., Corgne, A., Bureau, H., Ozawa, H., Garbarino, G., 2010.
725 Melting of peridotite to 140 GPa. Science 329, 1516-1518.

726 French, S.W., Romanowicz, B., 2015. Broad plumes rooted at the base of the Earth's
727 mantle beneath major hotspots. Nature 525, 95–99.

728 Garnero, E.J., Helmberger, D.V., 1998. Further structural constraints and uncertainties of
729 a thin laterally varying ultralow-velocity layer at the base of the mantle. J. Geophys. Res.
730 103 (B6), 12495-1250.

731 Garnero, E.J., McNamara, A.K., 2008. Structure and dynamics of Earth's lower mantle.
732 Science 230, 626-628.

733 Gasparik, T., 1990. Phase relations in the transition zone. J. Geophys. Res. 95, 15751-
734 15769.

735 Geballe, Z.M., Jeanloz, R., 2012. Origin of temperature plateaus in laser-heated diamond
736 anvil cell experiments. J. Appl. Phys. 111, 123518-1-15.

737 Hanfland, M., Syassen, K., Fahy, S., Louie, S.G., Cohen, M.L., 1986. The 1st-order Raman
738 mode of diamond under pressure. Physica B+C, 139 & 140B, 516-519.

739 Harvey, J.-P., Gheribib, A.E., Paul D. Asimow, P.D., 2015. A self-consistent optimization of
740 multicomponent solution properties: Ab initio molecular dynamic simulations and the
741 $MgO–SiO_2$ miscibility gap under pressure. Geochim. Cosmochim. Acta 161, 146–165.

742 Haselton, H.T., Newton, R.C., 1980. Thermodynamics of pyrope-grossular garnets and
743 their stabilities at high temperatures and high pressures. J.Geophys.Res. 85, 697306982.

744 Helffrich, G., 2006. Small-scale seismic heterogeneity and mantle structure. Astron.
745 Geophys. 47, 1.20-1.26.

746 Hirose, K., Fei, Y., Ma, Y., Mao, H.-K., 1999. The fate of subducted basaltic crust in the
747 Earth's lower mantle. Nature 397, 53-56.

748 Holland, T.J.B., Powell, P., 2011. An improved and extended internally consistent
749 thermodynamic dataset for phases of petrological interest, involving a new equation of
750 state for solids. J. Metamorph. Geol. 29, 333–383.

751 Karki, B.B., Bhattarai, D., Stixrude, L., 2007. First-principles simulations of liquid silica:
752 structural and dynamical behavior at high pressure. Phys. Rev. B, 76, 104205.

753 Labrosse, S., Hernlund, J.W., Coltice, N., 2007. A crystallizing dense magma ocean at the
754 base of the Earth's mantle. Nature 450, 866-869.

755 Lay, T., Hernlund, J., Buffett, B.A., 2008. Core-mantle boundary heat flow. Nat. Geosci. 1,
756 25-32.

757 Liebske, C., Corgne, A., Frost, D.J., Rubie, D.C. and Wood, B.J., 2005. Compositional effects
758 on element partitioning between Mg-perovskite and silicate melts. Contributions to
759 Mineralogy and Petrology 149, 113-128.

760 Liebske, C., Frost, D.J., 2012. Melting phase relations in the MgO–$MgSiO_3$ system between
761 16 and 26 GPa: Implications for melting in Earth's deep interior. Earth Planet. Sci. Lett.
762 345-348, 159–170.

763 Lord, O.T., Wann, E.T.H., Hunt, S.A., Walker, A.M., Santangeli, J., Walter, M.J., Dobson, D.P.,
764 Wood, I.G., Vočadlo, L., Morard, G., Mezouard, M., 2014a. The NiSi melting curve to 70
765 GPa. Phys. Earth Planet. Inter. 233, 13-23.

766 Lord, O. T., Wood, I. G., Dobson, D. P., Vočadlo, L., Wang, W., Thomson, A. R., et al. 2014b.
767 The melting curve of Ni to 1 Mbar. Earth Planet. Sci. Lett. 408, 226–236.

768 Mao, H.K., Xu, J., Bell, P.M., 1986. Calibration of the ruby pressure gauge to 800-kbar
769 under quasi-hydrostatic conditions. J. Geophys. Res. Solid Earth 91, 4673-4676.

770 McNamara, A., K., Zhong, S., 2005. Thermochemical structures beneath Africa and the
771 Pacific Ocean. Nature 437, 1136–1139.

772 Murakami, M., Ohishi, Y., Hirao, N., Hirose, K., 2012. A perovskitic lower mantle inferred
773 from high-pressure, high-temperature sound velocity data. Nature 485, 90–94.

774 Nakagawa, T., Tackley, P.J., 2008. Lateral variations in CMB heat flux and deep mantle
775 seismic velocity caused by a thermal-chemical-phase boundary layer in 3D spherical
776 convection, Earth Planet. Sci. Lett. 271, 348-358.

777 Nomura, R., Hirose, K., Uesugi, K., Ohishi, Y., Tsuchiyama, A., Miyake, A., Ueno, Y., 2014.
778 Low core-mantle boundary temperature inferred from the solidus of pyrolite. Science,
779 343, 522-525.

780 Petitgirard S., Malfait, W.J., Sinmyo, R., Kupenko, I., Hennet, L., Harries, D., Dane, T.,
781 Burghammer, M., Rubie, D.C., 2015. Fate of $MgSiO_3$ melts at core–mantle boundary
782 conditions. PNAS 112 (46), 14186–14190.

783 Pradhan, G.K., Fiquet, G., Siebert, J., Auzendea, A.-L., Morard, G., Antonangeli, D.,
784 Garbarino, G., 2015. Melting of MORB at core–mantle boundary. Earth Planet. Sci. Lett.
785 431, 247-255.

786 Presnall, D.C., Walter, M.J., 1993. Melting of forsterite, Mg_2SiO_4, from 9.7 to 16.5 GPa. J.
787 Geophys. Res. 98, B 11, 19,777-19,78.

788 Presnall, D.C., Weng, Y.-H., Milholland, C.S., Walter, M.J., 1998. Liquidus phase relations in
789 the system MgO–$MgSiO_3$ at pressures up to 25 GPa - constraints on crystallization of a
790 molten Hadean mantle. Phys. Earth Planet. Inter. 107 (1–3), 83–95.

791 Simon, F.E., Glatzel, G.Z., 1929. Remarks on fusion pressure curve. Zeitschrift für
792 Anorganische und Allgemeine Chemie, 178, 309-312.

793 Sinmyo, R., Hirose, K., 2010. The Soret diffusion in laser-heated diamond anvil cell. Phys.
794 Earth Planet. Inter. 180, 172-178.

795 Shen, G., Lazor, P., 1995. Measurement of melting temperatures of some minerals under
796 lower mantle pressures. J. Geophys. Res. 100 (B9), 17699-17713.

797 Solomatov, V. S., Stevenson, D. J., 1993. Kinetics of crystal growth in a terrestrial magma
798 ocean. J. Geophys. Res. 98 (E3), 5407-5418.

799 Stixrude, L., Karki, B.B., 2005. Structure and freezing of $MgSiO_3$ liquid in Earth's lower
800 mantle. Science 310, 297-299.

801 Stixrude, L., de Koker, N., Sun, N., Mookherjee, M., Karki, B.B., 2009. Thermodynamics of
802 silicate liquids in the deep Earth. Earth Planet. Sci. Lett. 278, 226–232.

803 Stixrude, L., Lithgow-Bertelloni C., 2011. Thermodynamics of mantle minerals - I.
804 Physical properties. Geophys. J. Int., 162, 610–632.

805 Tangney, P., Scandolo, S., 2002. An *ab initio* parametrized interatomic force field for
806 silica, J. Chem. Phys. 117, 8898-8904.

807 Tateno, S., Hirose, K., Ohishi, Y., 2014. Melting experiments on peridotite to lowermost
808 mantle conditions. J. Geophys. Res. Solid Earth 119, 4684-4694.

809 Thomas, C. W., Asimow, P. D., 2013. Preheated shock experiments in the molten
810 $CaAl_2Si_2O_8$-$CaFeSi_2O_6$-$CaMgSi_2O_6$ ternary: A test for linear mixing of liquid volumes at
811 high pressure and temperature. J. Geophys. Res. Solid Earth 118, 3354-3365.

812 Thompson, J.B. Jr., 1967. Thermodynamic properties of simple solutions. In: Researches
813 in Geochemistry (ed. Ableson, P.H.). New York, Wiley and Sons, 340 – 361.

814 Thomson, A.R., Walter, M.J., Lord, O.T., Kohn, S.C., 2014. Experimental determination of
815 melting in the system enstatite-magnesite and magnesite-calcite from 15 to 80 GPa. Am.
816 Mineral. 99, 1544-1554.

817 Thorne, M.S., Garnero, E.J., 2004. Inference on ultralow-velocity zone structure from a
818 global analysiss of SPdKS waves. J. Geophys. Res. B, 109, B08302:1-22.

819 Torsvik, T.H., Steinberger, B., Ashwal, L.D., Doubrovine, P.V., Trønnes, R.G., 2016. Earth
820 evolution and dynamics – a tribute to Kevin Bruke. Can. J. Earth Sci., 53, 1073-1087.

821 Trønnes, R.G., Frost, D.J., 2002. Peridotite melting and mineral-melt partitioning of major
822 and minor elements at 22–24.5 GPa. Earth Planet. Sci. Lett. 197, 117-131.

823 Walter, M.J., Koga, K.T., 2004. The effects of chromatic dispersion on temperature
824 measurement in the laser-heated diamond anvil cell. Phys. Earth Planet. Inter. 143 and
825 144, 541-558.

826 Walter, M.J., Nakamura, E., Trønnes, R.G., Frost, D., 2004. Experimental constraints on
827 crystallization differentiation in a deep magma ocean. Geochim. Cosmochim. Acta 68
828 (20), 4267 - 4284

829 Walter, M.J., Thomson, A.R., Wang, W., Lord, O.T., Ross, J., McMahon, S.C., Baron, M.A.,
830 Melekhova, E., Kleppe, A.K., Kohn, S.C., 2015. The stability of hydrous silicates in Earth's
831 lower mantle: experimental constraints from the systems MgO-SiO_2-H_2O and MgO-Al_2O_3-
832 SiO_2-H_2O. Chem. Geol. 418, 16-29.

833 Williams, Q., Garnero, E.J., 1996. Seismic evidence for partial melt at the base of earth's
834 mantle. Science, 273(5281), 1528-1530.

Wu, P., Eriksson, G., Peltonand, A. D., Blander, M., 1993. Prediction of the Thermodynamic Properties and Phase Diagrams of Silicate Systems – Evaluation of the FeO-MgO-$Si0_2$ System. ISIJ Int. 33 (1), 26-35.

Zerr, A., Boehler, R., 1993. Melting of (Mg,Fe)SiO_3-perovskite to 625 kilobars: Indication of a high melting temperature in the lower mantle. Science 262, 553-555.

Supplementary materials

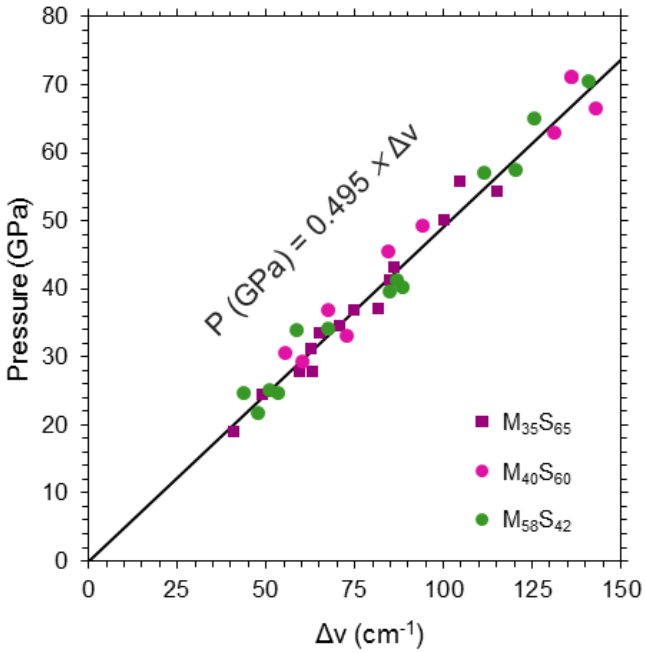

Figure S1. Calibration of the stress-induced Raman shift of the diamond singlet mode measured at the culet surface relative to pressure measured by ruby fluorescence, both measured after quenching. To calibrate the diamond peak shift, ruby was added to one of the sample chambers in many of our multi-chamber experiments. After laser heating we measured both the R1 ruby fluorescence peak from the ruby-bearing sample chamber and the Raman shift of the singlet peak from the diamond culet at the same position. Thomson et al. (2014) and Walter et al. (2015) found that the calibration can vary depending on the sample material and pressure media, therefore separate calibration curves for the different compositions were tested. The linear regressions for MgO-rich and SiO_2-rich samples resulted in slopes of 0.4937 and 0.4954 GPa/$(cm)^{-1}$, respectively, and are within uncertainty, therefore we fitted all the data points simultaneously yielding a slope of 0.495 GPa/$(cm)^{-1}$ when forced through the origin.

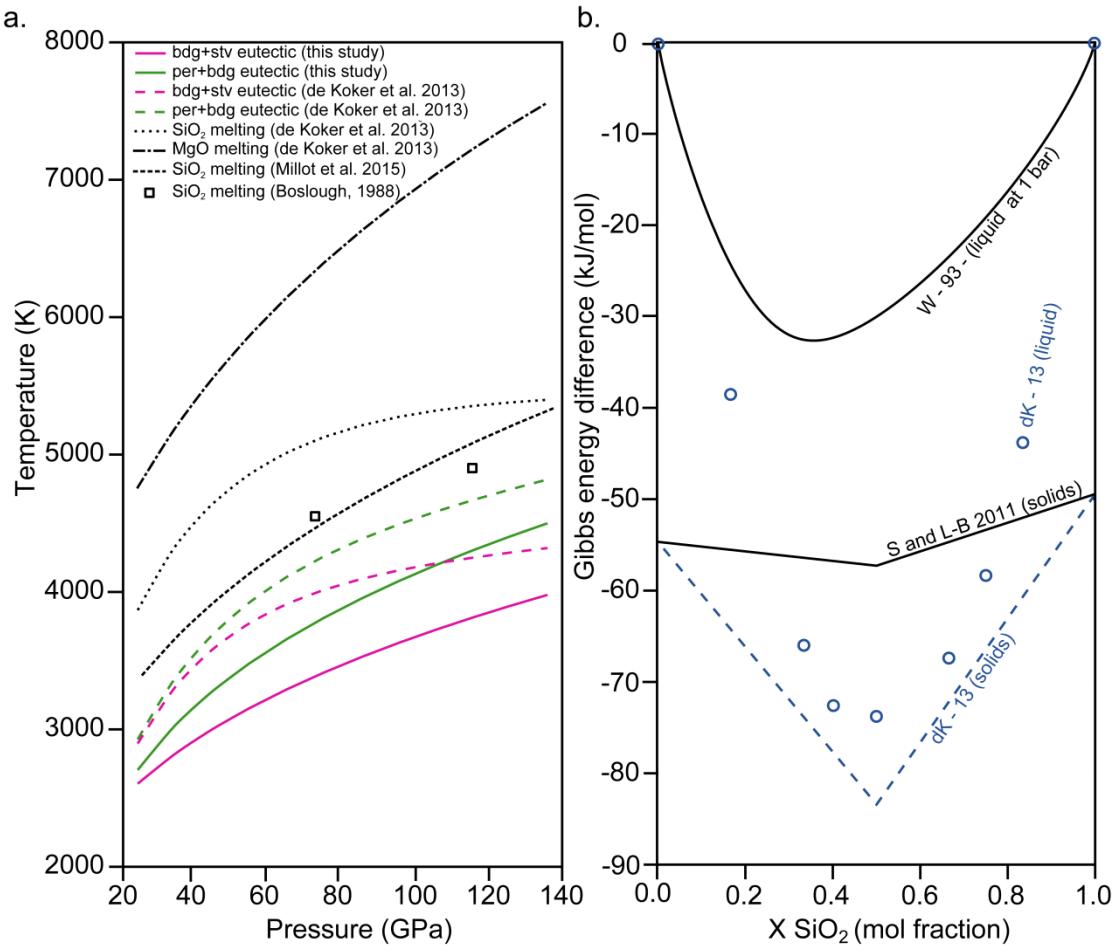

884

885

886 **Figure S2. (a)** The per + bdg (green solid line) and bdg + stv (pink solid line) eutectic
887 melting curves experimentally determined in this study and ab initio results by de Koker
888 et al. (2013; dashed lines) together with MgO and SiO_2 melting curves used in the
889 thermodynamic modelling by de Koker et al. (2013) and our calculations of MgO and
890 SiO_2 activities in the liquids. The endmembers melting curves were originally
891 determined by Koker and Stixrude (2009) and Karki et al. (2006) for MgO and Karki et
892 al. (2007) for SiO_2. Recently determined melting curve for SiO_2 based on shock data
893 extended to 500 GPa by Millot et al. (2015) and previous shock data by Boslough, 1988
894 suggests lower and steeper melting curve of SiO_2. **(b)** The difference in Gibbs energy of
895 solids and liquids at 24 GPa and 2605 K from de Koker et al. (2013) (dK - 13) study in
896 comparison with experimental datasets for solids by Stixrude and Lithgow-Bertelloni
897 (2011) (S and L-B - 2011) and 1 bar experimental liquid Gibbs free energy of mixing
898 curve from Wu et al. (1993) (W - 93).

899

900

Table S1. Experimental conditions and melting temperatures (K) in the MgO-$MgSiO_3$ sub-system.

C	Experiment	P (GPa)	T_{max}	σ	$T_{max,s}$	σ
$M_{58}S_{42}$	MB_E4_A	30,7	2831	65	2793	65
	MB_E4_D	44,3	3304	185	3323	184
	MB_E4_C	50,0	3603	91	3506	93
	MB_E9_A	20,4	2734	109	2705	161
	MB_E9_C	55,7	3509	15	3502	14
	MB_E10_D	32,7	3145	50	3142	50
	MB_E16_D	27,4	2782	101	2770	98
	MB_E18_A	35,4	3112	60	3071	63
	MB_E18_B	40,3	3193	56	3174	62
	MB_E18_C	47,8	3448	166	3433	156
	MB_E32	99,1	4161	131	4072	130
	MB_E33_A	69,8	3687	103	3637	112
	MB_E33_C	63,6	3630	91	3617	93
	MB_E33_B	77,4	4004	118	4013	175
	MB_E43_C	48,2	3164	57	3150	101
	MB_E43_B	54,1	subsolidus ~2400 K			
	MB_E43_A	58,0	subsolidus ~2150 K			
	MB_E43_D	50,7	long subsolidus ~1800 K (30 minutes)			
	MB_E48_C	58,2	3556	89	3484	93
	MB_E48_A	63,3	subsolidus ~2450 K			
	MB_E48_B	60,0	long subsolidus ~2200 (30 minutes)			
	MB_E50_C	40,1	3324	108	3291	102
	MB_E50_A	47,3	subsolidus ~2500 K			
	MB_E50_B	45,0	subsolidus ~2400 (30 minutes)			

913

914

Table S2. Experimental conditions and melting temperature (K) in the $MgSiO_3$–SiO_2 sub-system

C	Experiment	P (GPa)	T_{max}	σ	$T_{max,s}$	σ
$M_{35}S_{65}$	MB_E3_C	28,6	2757	36	2753	35
	MB_E5_A	23,1	2645	109	2640	108
	MB_E5_D	42,5	3112	94	3102	93
	MB_E5_C	45,3	2796	72	2784	47
	MB_E7_A	32,3	3004	45	2997	45
	MB_E29	108,5	3887	156	3852	271
	MB_E34	89,3	3448	289	3449	274
	MB_E37	91,4	3690	299	3675	304
	MB_E44_C	48,3	3038	186	3026	178
	MB_E44_B	53,3	subsolidus ~2350 K			
	MB_E44_A	49,1	subsolidus ~2300 K			
	MB_E44_D	44,8	long subsolidus ~2000 K (30 minutes)			
	MB_E47_B	80,0	subsolidus ~2900 K			
	MB_E47_C	86,1	subsolidus ~2450 K			
	MB_E47_A	78,3	long subsolidus ~2200 K (30 minutes)			
$M_{40}S_{60}$	MB_E8_D	30,6	2910	42	2894	38
	MB_E8_A	55,2	3066	74	3055	70
	MB_E8_B	67,0	3188	44	3162	39
	MB_E8_C	68,7	3472	42	3444	40
	MB_E11_A	21,7	2497	120	2486	115
	MB_E11_D	29,3	2719	128	2669	203
	MB_E11_B	43,7	2938	121	2930	124
	MB_E12_D	30,1	2982	82	2949	78
	MB_E12_B	51,3	3281	123	3269	116
	MB_E19_C	35,4	2938	323	2916	312
	MB_E19_A	77,2	3479	181	3468	177
	MB_E19_B	73,7	3151	60	3144	58
	MB_E22_A	42,7	2968	115	2957	112
	MB_E22_B	60,2	3334	105	3312	105
	MB_E36_A	37,8	2775	146	2760	141
	MB_E36_C	36,7	subsolidus ~2500 K			
	MB_E36_B	53,1	subsolidus ~2700 K			
	MB_E49_B	62,3	subsolidus ~2900 K			
	MB_E49_A	71,8	subsolidus ~2400 K			
	MB_E49_C	68,0	long subsolidus ~2700 K (30 minutes)			
	MB_E45_A	80,1	3625	51	3573	45
	MB_E45_B	80,8	subsolidus ~2400 K			
	MB_E45_C	81,3	long subsolidus ~2000 K (30 minutes)			

915

916

Table S3. Fitting parameters for the melting curves defined in this study

eutectic:	T_{24} (K)	A (GPa)	C
MgO-$MgSiO_3$	2705	19.156 ± 7.38	3.7796 ± 0.878
$MgSiO_3$-SiO_2	2605	29.892 ± 16.2	3.6770 ± 1.28

The Simon-Glatzel equation: $T_m = T_{24}\left(1 + \frac{P_m}{A}\right)^{\frac{1}{C}}$ (Simon and Glatzel, 1929)

References:

Boslough, M.B., 1988. Postshock temperatures in silica. J. Geophys. Res. 93 (B6), 6477-6484.

de Koker, N., Strixrude, L., 2009. Self-consistent thermodynamic description of silicate liquids, with application to shock melting of MgO periclase and $MgSiO_3$ perovskite. Geophys. J. Int. 178, 162–179.

de Koker, N., Karki, B.B., Stixrude, L., 2013. Thermodynamics of the MgO–SiO_2 liquid system in Earth's lowermost mantle from first principles. Earth Planet. Sci. Lett. 361, 58-63.

Karki, B.B., Bhattarai, D., Stixrude, L., 2006. First principles calculations of the structural, dynamical and electronic properties of liquid MgO. Phys. Rev. B 73, 174208.

Karki, B.B., Bhattarai, D., Stixrude, L., 2007. First-principles simulations of liquid silica: structural and dynamical behavior at high pressure. Phys. Rev. B 76, 104205.

Millot, M., Dubrovinskaia, N., Černok, A., Blaha, S., Dubrovinsky, L., Braun, D.G., Celliers, P.M., Collin, G.W., Eggert, J.H., Jeanloz, R., 2015. Shock compression of stishovite and melting of silica at planetary interior conditions. Science 418, 8–11.

Simon, F.E., Glatzel, G.Z., 1929. Remarks on fusion pressure curve. Zeitschrift für Anorganische und Allgemeine Chemie, 178, 309-312.

Stixrude, L., Lithgow-Bertelloni, C., 2011. Thermodynamics of mantle minerals - I. Physical properties. Geophys. J. Int., 162, 610–632.

940 Thomson, A.R., Walter, M.J., Lord, O.T., Kohn, S.C., 2014. Experimental determination of
941 melting in the system enstatite-magnesite and magnesite-calcite from 15 to 80 GPa. Am.
942 Mineral. 99, 1544-1554.

943 Walter, M.J., Thomson, A.R., Wang, W., Lord, O.T., Ross, J., McMahon, S.C., Baron, M.A.,
944 Melekhova, E., Klepp, A.K., Kohn, S.C., 2015. The stability of hydrous silicates in Earth's
945 lower mantle: experimental constraints from the systems MgO-SiO_2-H_2O and MgO-Al_2O_3-
946 SiO_2-H_2O. Chem. Geol. 418, 16-29.

947 Wu, P., Eriksson, G., Peltonand, A.D., Blander, M., 1993. Prediction of the Thermodynamic
948 Properties and Phase Diagrams of Silicate Systems – Evaluation of the FeO-MgO-$Si0_2$
949 System. ISIJ Int. 33 (1), 26-35.